THE JOURNAL OF BIOLOGICAL CHEMISTRY VOL. 283, NO. 50, pp. 35236–35246, December 12, 2008


# Specificity of Interactions between mDia Isoforms and Rho Proteins*

Received for publication, July 23, 2008, and in revised form, September 26, 2008 Published, JBC Papers in Press, September 30, 2008, DOI 10.1074/jbc.M805634200

**Michael Lammers, Simon Meyer, Dorothee Kühlmann, and Alfred Wittinghofer**[1]

*From the Max-Planck-Institute for Molecular Physiology, Department of Structural Biology, Otto-Hahn-Strasse 11, 44227 Dortmund, Germany*

**Formins are key regulators of actin nucleation and polymerization. They contain formin homology 1 (FH1) and 2 (FH2) domains as the catalytic machinery for the formation of linear actin cables. A subclass of formins constitutes the Diaphanous-related formins, members of which are regulated by the binding of a small GTP-binding protein of the Rho subfamily. Binding of these molecular switch proteins to the regulatory N-terminal $mDia_N$, including the GTPase-binding domain, leads to the release of auto-inhibition. From the three mDia isoforms, mDia1 is activated only by Rho (RhoA, -B, and -C), in contrast to mDia2 and -3, which is also activated by Rac and Cdc42. Little is known about the determinants of specificity. Here we report on the interactions of RhoA, Rac1, and Cdc42 with mDia1 and an mDia1 mutant ($mDia_N$-Thr-Ser-His (TSH)), which based on structural information should mimic mDia2 and -3. Specificity is analyzed by biochemical studies and a structural analysis of a complex between Cdc42·Gpp(NH)p and $mDia_N$-TSH. A triple NNN motif in mDia1 (amino acids 164–166), corresponding to the TSH motif in mDia2/3 (amino acids 183–185 and 190–192), and the epitope interacting with the Rho insert helix are essential for high affinity binding. The triple N motif of mDia1 allows tight interaction with Rho because of the presence of Phe-106, whereas the corresponding His-104 in Rac and Cdc42 forms a complementary interface with the TSH motif in mDia2/3. We also show that the F106H and H104F mutations drastically alter the affinities and thermodynamics of mDia interactions.**

The dynamics of the actin cytoskeleton play an important role in many physiological processes, *e.g.* cytokinesis, cell migration, cell morphology, and phagocytosis (1–3). Although the Arp2/3 complex leads to the formation of a branched actin network and is regulated by WASP and VASP and others, the formins and the protein Spire catalyze the nucleation and polymerization of unbranched actin filaments (3–8). Formins are multidomain proteins characterized by formin homology domains. All formins contain the FH2[2] domain, the actual catalytic machinery for actin polymerization, which is often in tandem with FH1, a polyproline domain mediating profilin·actin recruitment (9–13). The FH3 domain is believed to play a role in the subcellular localization of the protein and is the least conserved FH domain (12, 14–16).

The formins are subdivided into seven groups as follows: Dia (diaphanous), DAAM (dishevelled-associated activator of morphogenesis), FRL (formin-related gene in leukocytes), FHOD (formin homology domain-containing protein), INF (inverted formin), FMN (formin), and delphilin (24). The structure of the FH2 domain from yeast and mouse showed a doughnut-shaped all-helical molecule, which forms a dimer binding with high affinity to actin (13, 17–21). From the structure of the FH2 alone and in complex with tetramethylrhodamine-labeled actin and from biochemical experiments, the mechanism of actin polymerization by the formin was described as a stair-stepping mechanism, where the FH2 dimer binds to the barbed ends of actin filaments as a leaky capper that processively catalyzes barbed-end actin assembly (11, 13, 17, 22–28). The processive movement could be shown *in vitro* as well as *in vivo* (11, 22, 23).

For most formins, the tandem arrangement of FH1-FH2 domains is necessary for function. FH1 contains several stretches of poly-L-prolines that are targets for Src homology 3 and WW domain-containing proteins and for profilin (19, 29, 30). By binding to G-actin as well as to FH1, profilin delivers actin monomers to the barbed end of the filament and increases the concentration of actin near the FH2 domain (13, 28). Therefore, FH1-FH2 accelerates the association rate for ATP-G-actin monomers at the barbed end, but it also accelerates the hydrolysis rate of actin-bound ATP (11, 22). This leads to the release of profilin from the barbed-end making this site accessible for the next round of G-actin incorporation (11).

N-terminal to the FH1/FH2 domains, the subclass of Diaphanous-related formins contains a regulatory unit consisting of the GBD and FH3 domains ($mDia_N$ in short), which interact with the C-terminal Diaphanous-autoregulatory domain (DAD) (31–36). The deletion of either GBD or DAD leads to a constitutively active protein that induces actin stress fibers and serum-response factor-dependent nuclear transcription (25, 37–39). The *Drosophila* protein Diaphanous was isolated in *Drosophila* as a gene involved in cytokinesis. There are three

* The costs of publication of this article were defrayed in part by the payment of page charges. This article must therefore be hereby marked "*advertisement*" in accordance with 18 U.S.C. Section 1734 solely to indicate this fact.

*The atomic coordinates and structure factors (code 3EG5) have been deposited in the Protein Data Bank, Research Collaboratory for Structural Bioinformatics, Rutgers University, New Brunswick, NJ (http://www.rcsb.org/).*

[1] To whom correspondence should be addressed. Tel.: 49-231-133-2100; Fax: 49-231-133-2199; E-mail: alfred.wittinghofer@mpi-dortmund.mpg.de.

[2] The abbreviations used are: FH, formin homology; Bistris propane, 1, 3-bis[tris(hydroxymethyl)methylamino]propane; GBD, GTPase-binding domain; Dia, Diaphanous; mant, *N*-methylanthraniloyl; Gpp(NH)p, guanosine 5′-($\beta,\gamma$-imido)triphosphate; ARR, Armadillo repeat region; DID, Diaphanous-inhibitory domain; DAD, Diaphanous-autoregulatory domain; ARM, Armadillo repeat motif; DCR, DAD core region; GNBP, guanine nucleotide-binding protein; PDB, Protein Data Bank; ITC, isothermal titration calorimetry; WT, wild type; ROCK, Rho-associated coiled-coil kinase.

mammalian homologues mDia1–3 and two Diaphanous-related formin proteins Bni1p and Bnr1p in *Saccharomyces cerevisiae* (12). Binding of activated small GTP-binding proteins from the Rho family leads to the release of the inhibitory interaction between DAD and $mDia_N$ and activation of the FH2 that is not yet completely understood (31–33, 35, 40).

It has been shown by us and others that $mDia_N$ consists of three subdomains as follows: $GBD_N$, Armadillo repeat region (ARR) also called DID (Diaphanous-inhibitory domain), and dimerization domain (Dim) (33, 35, 40). The structure of the $mDia_N$ in complex with activated RhoC shows that Rho interacts via switch I and II with the GBD but also with the ARR via the Rho insert helix. The DAD-binding site on $mDia_N$ (DID) has also been described biochemically and structurally (32). The structure shows that the 16 highly conserved residues of the DAD core region (DCR) form an $\alpha$-helix, which binds to the ARR in a site not directly overlapping with the Rho-binding site (32, 41). Nevertheless, Rho actively dissociates DAD from its binding site via long range electrostatic repulsion and short range steric clashes (32).

Small guanine nucleotide-binding proteins (small GNBP, G proteins) cycle between a GDP-bound inactive form and a GTP-bound active form (42–44). They interact with their effector proteins preferentially in the GTP-bound form (44, 45). This discrimination is because of the conformation of two loop regions, switch I and II, that adopt a defined conformation when connected to the $\gamma$-phosphate. Rho proteins interact with a number of different effectors, which in turn regulate the actin cytoskeleton either directly, as with mDia, or indirectly by modifying the activity of actin-binding proteins (44, 46–53). Binding motifs in Rho effectors are divergent, with a Cdc42/Rac-interactive binding motif in Cdc42/Rac effectors WASP, WAVE, ACK, and PAK (47, 54). The Rho effectors Rhophilin, Rhotekin, and protein kinase N, and ROCK bind via an antiparallel coiled-coil motif (47, 55, 56), whereas mDia binding to Rho is again via a different structural motif (35). The common feature of these interactions is that Rho proteins not only recruit their effectors to a particular membrane site but that they also allosterically activate the effector (5, 47, 57). This involves the release of an intramolecular autoinhibited state that can be found in the cases of kinases, *e.g.* ROCK, protein kinase N, or PAK, but also in the case of WASP, WAVE, and mDia1 (47). For mDia1 the release of autoinhibition by Rho binding does not lead to full activation of the actin polymerization activity catalyzed by FH2 (25, 40).

The activation of Rho proteins plays an important role in spatio-temporal regulation of the actin cytoskeleton inside the cell. Very often, different signal transduction pathways via Rho proteins lead to similar or overlapping cellular responses (58). Effectors of Rho proteins are nevertheless not promiscuous in responding to either Rho and its homologues, *i.e.* RhoA, -B, -C, or to Cdc42 and Rac and its homologues such as TC10. Because a particular Rho protein interacts with a number of structurally different effectors via the highly conserved switch I and II regions, a high plasticity in the interface is required (59). Numerous Rho family effectors have been described so far, defined as proteins that only bind to the GTP-bound state. ROCK I and II and Rhotekin specifically interact with and are activated by binding of Rho but not Rac or Cdc42 (39, 60). It has been postulated that for ROCK II only residue Glu-40 of RhoA is important for discriminating between RhoA, Cdc42, and Rac1 (61). The Cdc42/Rac-interactive binding motif containing proteins PAK, WASP, and WAVE and others are specific effectors for members for either Rac or Cdc42 but do not interact with Rho.

In case of mDia, the situation is different in that mDia1 specifically binds to and is activated by RhoA, -B, and -C (39), whereas mDia2 and -3 seem to be highly promiscuous and activated by RhoA-C, Cdc42, and RhoD (36, 39, 62, 63). The question to ask is whether, like in protein kinase C-related kinase, the effector binds to multiple Rho family members at different binding sites or whether different G proteins use the same binding site. Here we analyzed the specificity of interaction between mDia isoforms and Rho proteins. We show that Rho, Rac, and Cdc42 use a similar binding site and that most of the specificity is determined by a Asn-Asn-Asn (triple N) motif of mDia1 that is replaced by Thr-Ser-His (TSH) in mDia2 and -3. On the Rho site, specificity is determined by a Phe-His substitution of Phe-106. We also observe for the first time that the insert helix, a specific hallmark of Rho proteins, is involved in effector binding and specificity.

## EXPERIMENTAL PROCEDURES

*Recombinant Proteins*—Proteins were expressed as glutathione *S*-transferase fusions using the vector pGEX-4T1 (Amersham Biosciences). All proteins were expressed in *Escherichia coli* BL21(DE3) cells. Cells were grown to an $A_{600}$ of 0.7 (37 °C, 160 rpm) and induced with 100 $\mu$M isopropyl $\beta$-D-thiogalactopyranoside overnight at 20 °C for $mDia_N$ and $mDia_N$-TSH and at 18 °C for RhoA, Rac1, and Cdc42. Cells were harvested and resuspended in buffer A (20 mM Tris/HCl, pH 7.5, 100 mM NaCl, 2 mM $\beta$-mercaptoethanol, and 5 mM $MgCl_2$ in cases of RhoA, Rac1, and Cdc42) containing 0.1 mM phenylmethylsulfonyl fluoride and 2 mM EDTA. Cells were lysed by microfluidizing; the extract was applied to a GSH-Sepharose column (Amersham Biosciences), and the column was washed with buffer B (20 mM Tris/HCl, pH 7.5, 100 mM NaCl, 2 mM $\beta$-mercaptoethanol, 5 mM $MgCl_2$). The fusion protein was digested with 5 units of thrombin (Serva) per mg of glutathione *S*-transferase fusion protein on the column overnight at 4 °C. Final purification was done with size exclusion chromatography in buffer B using a Superdex S200 for $mDia_N$ and $mDia_N$-TSH or S75 for RhoA, Rac1, and Cdc42.

Point mutations were made using the QuikChange method of Stratagene. Mutant proteins were purified like the wild type proteins. Concentrations of $mDia_N$ and $mDia_N$-TSH were determined using the absorption at 280 nm under denaturing conditions with the extinction coefficient deduced from the sequence, and RhoA/Cdc42/Rac1 concentrations were determined by the Bradford assay. Rho was purified and loaded with Gpp(NH)p and mant-Gpp(NH)p as described elsewhere (35). Rac1 and Cdc42 were purified using the same strategy.

*Stopped-flow Kinetics*—The experiments were done at 20 °C using a SX18 MW Applied Photophysics apparatus (Leatherhead, UK). The mant fluorophore (Molecular Probes) was excited at 366 nm with a bandpass of 6.4 nm. Emission (at 450

nm) was recorded using a 408-nm cutoff filter. All measurements were done with a final concentration of 100 nM mant-Gpp(NH)p-loaded GNBP/mutated GNBP. Increasing concentrations of wild type or mutant $mDia_N$ (1–15 $\mu$M) were used in the experiments using pseudo first-order conditions. The observed fluorescence transients were fitted to a single exponential function to obtain $k_{obs}$. The association rate constant $k_{on}$ was derived from the slope of $k_{obs}$ *versus* protein concentration. The dissociation rate constants were obtained by mixing a preformed 100 nM $mDia_N$·RhoA·mant-Gpp(NH)p (or mutated proteins) complex with a 100-fold excess of unlabeled Rho protein. All measurements were done in buffer C (300 mM NaCl, 50 mM Tris/HCl, pH 7.5, 2 mM $\beta$-mercaptoethanol, 5 mM $MgCl_2$), which in experiments with RhoA additionally contained 5 mM $MgCl_2$. GraFit 3.0–5.0 was used for data analysis.

*ITC Measurements*—The interaction of $mDia_N$/$mDia_N$-TSH and RhoA/Cdc42/Rac1 and DAD-(1145–1200) and mutants was done by ITC based on Wiseman *et al.* (64) (MicroCal™; VP-ITC MicroCalorimeter). All measurements were carried out in buffer B at 20 °C. DAD, RhoA, Cdc42, and Rac1 (or mutants) (syringe) were stepwise-injected to the $mDia_N$, $mDia_N$-TSH solution (cell). The heating power per injection was observed over the reaction time until equilibrium was reached. The data were analyzed using the software provided by the manufacturer.

*Crystallization, Data Collection, and Structure Solution*—Crystals of the $mDia_N$[TSH] domain (69–451) in complex with Cdc42-(1–178)·Gpp(NH)p were grown in buffer D containing Bistris propane, pH 8.8 (pH adjusted with citric acid), 26% PEG3350, 250 mM sodium tartrate to a size of ~100 × 200 × 100 $\mu$M using the hanging drop/vapor diffusion method. The protein was solved in buffer B containing 100 mM NaCl, 20 mM Tris/HCl, pH 7.5, 2 mM $\beta$-mercaptoethanol, and 5 mM $MgCl_2$. 1 $\mu$l of protein solution of various concentrations (2.5, 5, and 10 $\mu$g/$\mu$l) was mixed with the reservoir solution. After 1 day crystals were grown to their final size and flash-frozen in liquid nitrogen using reservoir solution with 35% PEG3350 as cryoprotectant.

Data set collection has been performed at the Swiss Light Source, Paul Scherrer Institut, Villigen, Switzerland (Table 4). The native dataset was collected at 100 K on beam line PXII at a wavelength of 0.95 Å using a Mar225 CCD detector. Data were indexed, integrated, and scaled with the XDS package (65).

Initial phases were obtained by molecular replacement with the program Molrep (66) using the $mDia_N$·RhoC (PDB code 1Z2C) as a search model. The initial solution containing two Cdc42·Gpp(NH)p·$mDia_N$-TSH complexes per asymmetric unit was subjected to crystallographic simulated annealing as implemented in CNS (67). The program Coot (68) was used to build the model into the $2F_o - F_c$ and $F_o - F_c$ maps in iterative rounds of NCS refinement, including translation, liberation, and screw-rotation parameters with REFMAC (69). The final model has a good geometry with 100% of all residues in the allowed regions of the Ramachandran plot as judged by the Molprobity server (70). A summary of data collection and refinement statistics is given in Table 4. Figures of molecular structures were prepared with PyMOL (71).

*Coordinates*—The structure factors and coordinates have been deposited at the PDB with PDB code 3EG5.

## RESULTS

*Specificity of the DAD-N-terminal Auto-inhibitory Interaction*—Activation of mDia1 involves binding of Rho·GTP, which actively dissociates the interaction between the regulatory N terminus and the C-terminal DAD of mDia1 (32) (see Fig. 1*A* for domain organization of mDia1). The crystal structure of the [$mDia_N$·DAD] complex showed that the DCR (see Fig. 1*B* for an alignment of DCRs) forms an $\alpha$-helix that interacts mainly via hydrophobic interactions with the ARR of $mDia_N$ and that the binding sites of DAD and RhoA·Gpp(NH)p on $mDia_N$ are partially overlapping such that a ternary complex cannot be formed (32). Although the C-terminal basic region $^{1196}$RRKRG$^{1200}$ of DCR is not visible in the crystal structure (32), its deletion in DAD-(1145–1200) reduces the affinity toward $mDia_N$ 73-fold to 8 $\mu$M (Fig. 1*C*), as determined by ITC. To exclude that this extra part of DAD interferes with the Rho-binding site and thereby contributes to specificity, we tried to locate the binding site for the basic region of DAD in $mDia_N$. We reasoned that a negatively charged patch near the third helix of ARM5 and the Dim domain could represent the binding site of the basic motif. Single, double, and triple mutants of acidic residues were introduced (E358R, E358R/E362R, and E358R/E362R/E366R, respectively), and binding of the mutant constructs toward DAD-(1145–1200)was followed by ITC. Although only marginal effects on affinity could be measured for the single point mutation (E358R), an additive effect on affinities is observed for the single, double, and triple mutant (388 nM, 1.01 $\mu$M, and 2.15 $\mu$M) (Fig. 1*C*) with the affinities converging to the value measured for the DAD construct lacking the C-terminal basic region. These experiments clearly establish that the C-terminal basic region of DAD interacts with the negatively charged patch located on $mDia_N$ remote from the Rho-binding sites (Fig. 1*D*). Thus, an involvement of this part of DAD in generating specificity toward activated Rho proteins appears unlikely.

*Major Specificity Determinants*—By analyzing the RhoC·$mDia_N$ complex structure and comparing them to the sequence of mDia2 and -3, we identified a triple Asn motif (Asn-164–166) of mDia1 in the central portion of the interface, which is replaced by TSH in mDia2/3 (Fig. 2, *A* and *C*). Asn-165 and Asn-166 are located in the loop connecting ARM1 (ARM is Armadillo repeat motif) and ARM2 of the ARR of $mDia_N$ and are apparently required for the correct positioning of the Arg-$68^R$ (throughout the whole text, superscripts R, C, NNN, and TSH indicate residues of Rho, Cdc42, wild type $mDia_N$-NNN, and mutated $mDia_N$-TSH, respectively), a residue being highly crucial for the binding because it wedges deeply into the space between the $GBD_N$ and ARR subdomains of $mDia_N$ (35) (Fig. 2*C*). From the residues of Rho that are in interaction distance with the triple Asn motif only, Phe-106 is variant among Rho, Rac, and Cdc42, and in the latter two it is replaced by His (Fig. 2, *B* and *C*). This together with our previous finding that mutation of F106H in Rho drastically reduces the affinity to mDia1 (35) argue for Phe-106 of Rho and His-104 of Cdc42/Rac being major determinants of affinity and probably specificity on the G

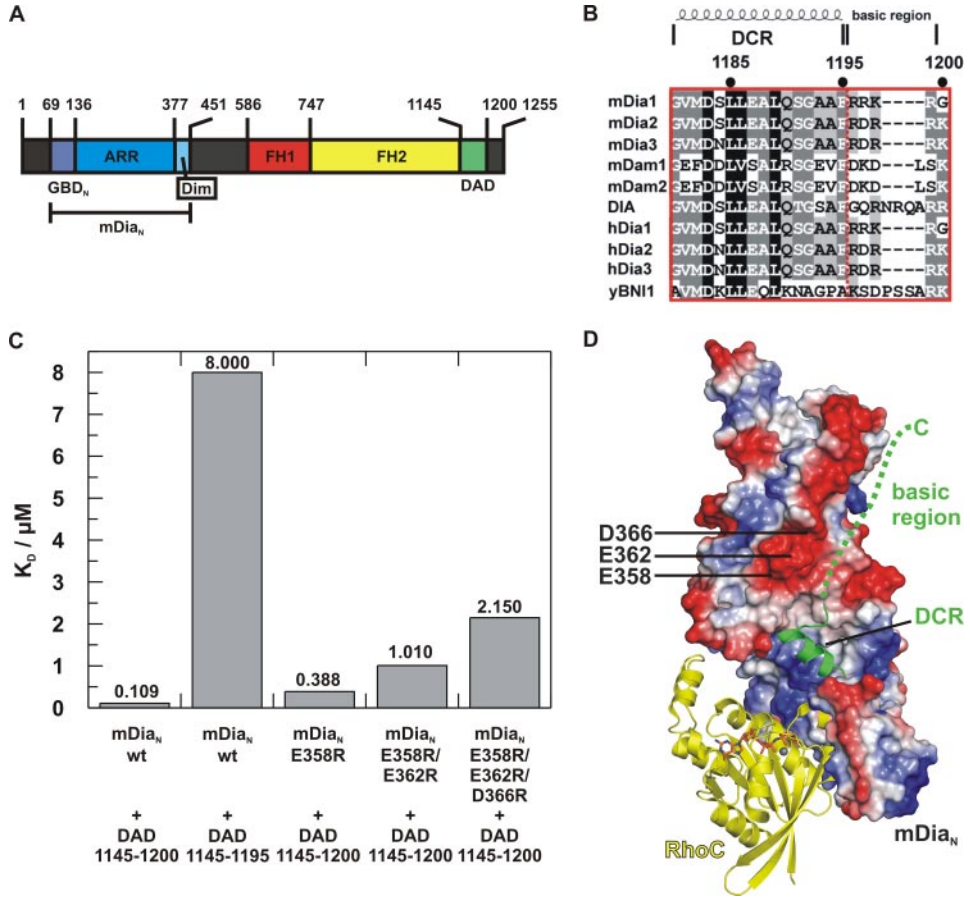


FIGURE 1. **Localization of the DAD on mDia.** *A,* schematic representation of the domain organization of mDia1, with *GBD$_N$*, GTPase-binding domain; *ARR*, Armadillo-repeat region; *Dim*, dimerization domain; *FH1–2*, Formin homology domains 1–2; *DAD*, Diaphanous autoregulatory domain; *mDia$_N$*, the N-terminal regulatory region. *B,* sequence alignment of DAD-core region (*DCR*) and basic region from different genes and organisms (SwissProt accession numbers in *parentheses*): *mDia1–3*, mouse (O08808, Q9Z207, and O70566); *mDam1–2*, mouse (Q8BPM0 and Q80U19); *Dia*, *Drosophila* (P48608); *hDia1–3*, human (O60610, O60879, and Q9NSV4); *yBNI1*, *S. cerevisiae* (P41832). 100% conserved, *black-shaded*; 80% conserved, *dark gray*; 60% conserved, *light gray*. *C,* equilibrium dissociation constants ($K_D$) (from ITC) for WT and mutant DAD constructs as indicated. *D,* model of the ternary mDia$_N$·RhoC·DAD complex obtained by superimposition of the mDia$_N$·DAD complex (PDB 2BAP) with the RhoC·mDia$_N$ complex structure (1Z2C), with mDia$_N$ shown in electrostatic surface representation (*blue* for positively charged surfaces, *red* for negatively charged surfaces, and *white* for neutral surfaces). Residues Glu-358, Asp-362, and Glu-366 of mDia$_N$ are indicated. RhoC and the DAD core are displayed as *yellow* and *green ribbons*, respectively, Gpp(NH)p as *stick* model, and $Mg^{2+}$ as *sphere*. The *green dashed line* represents the course of the C-terminal basic region of DAD as suggested from data described in the text.

protein site. Because constructs of mDia2 and -3 were not available in soluble form, we mutated the mDia triple Asn motif to Thr-Ser-His (termed mDia$_N$-TSH) to produce a mimic of mDia2 and mDia3 for studying its influence on specificity of Rho family proteins to mDia isoforms.

Although the interaction between RhoA (bound to Gpp(NH)p) and mDia$_N$ could previously not be detected by isothermal titration calorimetry (ITC) under high salt conditions (300 mM NaCl, see "Experimental Procedures"), a $K_D$ of 9 nM could conveniently be determined at low salt, with favorable values for enthalpy and entropy (Fig. 3*A* and Table 2). This is very similar to what was previously found by stopped-flow fluorescence measurements under high (35) or low salt,[3] indicating that the affinity is not salt-sensitive in contrast to the enthalpy of the reaction. Furthermore, insertion of the TSH motif into mDia$_N$ did not affect its binding affinities to DADs of mDia1, mDia2, and mDia3, as confirmed by ITC (Table 1). We then investigated binding of RhoA, Rac1, or Cdc42 to mDia$_N$ and mDia$_N$-TSH using ITC (Fig. 3 and Table 2). Whereas mutation of the triple N motif to TSH does not change the affinity toward RhoA (9 nM) (Fig. 3, *A* and *B*), it increases affinity toward Cdc42 and Rac1 such that it becomes easily measurable (Fig. 3, *C* and *D*). Although the interaction of RhoA toward either mDia$_N$ or mDia$_N$-TSH is highly exothermic, driven by both enthalpy and entropy, the interactions of Cdc42 and Rac1 toward mDia$_N$ or mDia$_N$-TSH, are endothermic, with a compensating favorable entropy. As a control we also measured binding of DAD-(1145–1200) to mDia$_N$-TSH, which was basically unperturbed as compared with WT, an endothermic enthalpy, and a $K_D$ of 115 nM (Table 1).

We further assayed via ITC the influence of the Phe-106 to His substitution in Rho and of His-104 to Phe in Rac1 and Cdc42 on binding to mDia$_N$ and mDia$_N$-TSH. Mutation of Phe-106 to His in RhoA leads to 20-fold reduced affinity to mDia$_N$ and to a drastically reduced affinity to mDia$_N$-TSH ($K_D$ = 1418 nM), whereas wild type RhoA has an equal affinity to both mDia$_N$ and mDia$_N$-TSH ($K_D$ = 9 nM in both cases). For Rac1 and Cdc42 the exchange of His-104 with the more hydrophobic Phe in turn increases the affinities of Cdc42 and Rac toward mDia1$_N$ by 55- and 28-fold, respectively, and is similar with either the triple N or TSH motif (Fig. 3, *E* and *F*, and Table 2).

A notable feature of the His-Phe substitutions is that introduction of Phe dramatically alters the enthalpy of the binding reaction (Fig. 3 and Table 2). For Rac1 and Cdc42, the H104F mutation shifts the reaction enthalpy of binding from endothermic to exothermic, with a difference in $\Delta H$ of between 3.7 and 4.6 kcal/mol, irrespective of whether wild type or mDia$_N$-TSH is used. Although this leads to an increase in affinity, it is still partly diminished by a decrease in favorable (positive) entropy of $\Delta G$ of 1.5–2.2 kcal/mol, an effect often observed in protein-protein interactions as the so-called enthalpy-entropy compensation (72). For RhoA the opposite F106H exchange is less dramatic, with a decrease in favorable enthalpy of 1.4 (for WT) and 2 kcal/mol (for TSH), and does not significantly modify the entropy term of the binding reaction. This, at least in part, explains why RhoA shows the highest affinity to both

[3] M. Lammers, unpublished data.

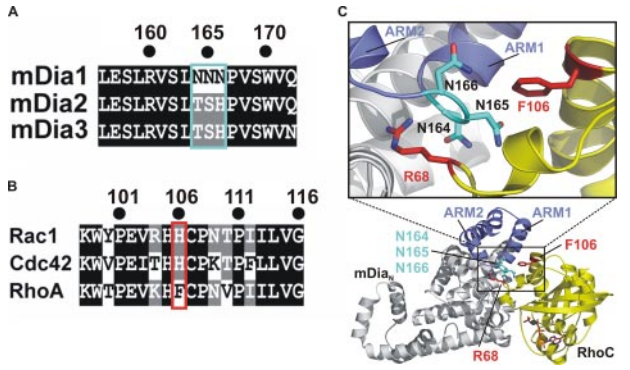


FIGURE 2. *A,* sequence alignment of mDia isoforms 1–3 (SwissProt accession numbers O08808, Q9Z207, and O70566, respectively) in the region of the triple NNN- and TSH motifs of mDia1, -2, and -3. *B,* sequence alignment of mouse Rac1, Cdc42, and RhoA (SwissProt accession numbers P63001, P60766, and Q9QUI0, respectively) in the region around Phe-106 of RhoA. *C,* ribbon diagram (*lower part*) of the structure of the RhoC·mDia$_N$ complex (PDB 1Z2C) with a blowup (*upper part*) highlighting the residues crucial for specificity, with Arg-68 and Phe-106 of RhoC and the triple NNN motif Asn-164–166 of mDia$_N$ located in a loop between ARM1 and ARM2, with mDia$_N$ as *gray ribbons*, ARM1 and ARM2 highlighted in *blue*, Asn-164–166 of as *cyan sticks*, RhoC as *yellow ribbons*, Arg-68 and Phe-106 as *red sticks,* and Gpp(NH)p·$Mg^{2+}$ as *orange sticks*.

mDia$_N$ and mDia$_N$-TSH compared with Rac1(H104F) and Cdc42(H104F). Rho binding is tighter because of favorable enthalpy and entropy contributions.

*Rho Insert Helix and Specificity*—From the biochemical experiments presented above, it is obvious that the specificity and affinity of the interactions between mDia isoforms and Rho subfamily members is not entirely due to the central contact point located between the GBD and ARR subdomains of mDia. A particular structural feature of Rho proteins is an extra helix located between the fifth $\beta$-strand and the fourth $\alpha$-helix of the canonical Ras fold, the so-called Rho insert helix (Fig. 4). In the crystal structure of the Rho·mDia complex, the Rho insert helix is close enough to the interface to assume a contribution to the interaction (Fig. 4*A*). Residues in direct contact distance (cutoff level 3.6 Å) include Lys-133$^{R}$ and Met-134$^{R}$ from one partner and Glu-345$^{NNN}$ and Asn-346$^{NNN}$ from the other partner. The interaction is mediated via a salt bridge between Lys-133$^{R}$ and Glu-345$^{NNN}$, which then enables Met-134$^{R}$ and Asn-346$^{NNN}$ to come into van der Waals interaction distance. Although not directly involved in the interaction with Rho, Ile-299$^{NNN}$ appears to play a crucial role in stabilizing the spatial integrity of the insert helix-binding site via a long range hydrophobic interaction with Ile-344$^{NNN}$, which then can correctly position Glu-

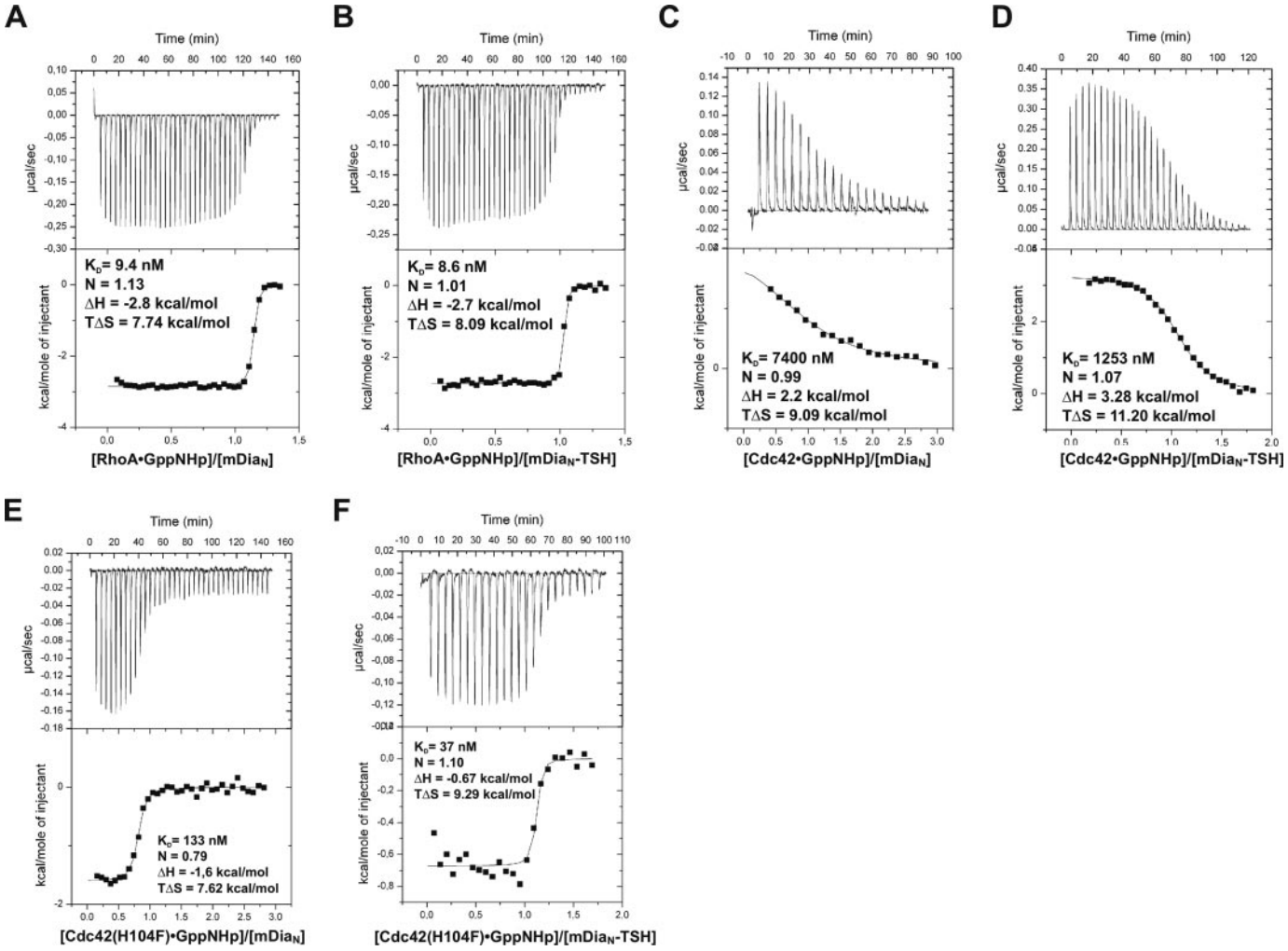


FIGURE 3. **ITC analysis of the interaction between WT and mutant Rho and mDia proteins, with RhoA·Gpp(NH)p and mDia$_N$ (*A*), RhoA·Gpp(NH)p and mDia$_N$-TSH (*B*), Cdc42·Gpp(NH)p and mDia$_N$ (*C*), or mDia$_N$-TSH (*D*) and Cdc42(H104F)·Gpp(NH)p and mDia$_N$ (*E*) or mDia$_N$-TSH (*F*).**

345$^{NNN}$ and Asn-346$^{NNN}$. Strikingly, there is considerable sequence variability for the residues involved in this interaction among Rho proteins and mDia isoforms (Fig. 4, *B* and *C*). Although Asn-346$^{NNN}$ is completely conserved among mDia1, -2, and -3, Glu-345 present in both mDia1 and -2 (Glu-368) is replaced by Lys (Lys-360) (Fig. 4*B*) in mDia3. Lys-133 of Rho is also present in Cdc42 (Lys-131), whereas Rac1 has a Glu-131 at this position. Met-134 of Rho in turn is replaced by Asn-132 in Cdc42 and by Lys-132 in Rac1 (Fig. 4*C*).

We thus studied the influence of residues involved in this interaction via stopped-flow binding kinetics (results are summarized in Table 3). Replacing the positively charged Lys-133$^{R}$ by a negatively charged Glu to disrupt the salt bridge with Glu-345$^{D}$ results in an 8-fold decreased affinity caused by an 8-fold decrease in the association rate constant $k_a$. Surprisingly, mutation of Glu-345$^{D}$ to Lys shows only a very small decrease in affinity to RhoA. Mutation of Met-134$^{NNN}$ to Glu decreases the affinity of Rho to mDia$_N$ by a factor of 2, whereas mutation of Met-134$^{NNN}$ to Ala has no effect implying that electrostatic repulsion between the negative charges of M134E$^{R}$ and Glu-345$^{NNN}$ has more impact on the affinity than the decreased hydrophobic interactions resulting from the M134A$^{R}$ exchange. Mutation of Lys-135$^{R}$, conserved among Rho proteins but not directly involved in the interaction, to Ala and to Glu does not show an effect on binding. Interestingly, mutation of Ile-299$^{NNN}$, which does not directly interact with RhoC in the crystal structure, to either Ala or Glu drastically reduces the affinity to Rho by 3000- and 7000-fold, respectively, which is mainly due to a 2250- and 3600-fold increase in the dissociation rate constant, respectively. Because binding of DAD is not affected by the Ile-299$^{NNN}$ mutations as confirmed by ITC measurements (data not shown), we conclude that the Ile-299$^{NNN}$ mutations disturb the local structural integrity of the interface to the Rho insert helix.

**TABLE 1**

**Thermodynamic analysis by ITC of binding of DAD from mDia1, -2, and -3 to WT and TSH mDia$_N$**

*N* is the stoichiometry of binding.

| Construct | $K_D$, nM | ΔH/kcal·mol$^{-1}$ | TΔS/kcal·mol$^{-1}$ | *N* |
|---|---|---|---|---|
| **mDia$_N$** | | | | |
| DAD$_{mDia1}$[a] | 109 ± 10 | 10.16 ± 0.053 | 19.49 | 0.92 |
| DAD$_{mDia2}$[a] | 325 ± 20 | 6.87 ± 0.040 | 15.57 | 0.99 |
| DAD$_{mDia3}$[a] | 277 ± 23 | 6.65 ± 0.045 | 15.45 | 1.10 |
| **mDia$_N$-TSH** | | | | |
| DAD$_{mDia1}$[a] | 115 ± 5 | 6.45 ± 0.016 | 15.74 | 0.88 |
| DAD$_{mDia2}$[a] | 322 ± 25 | 5.08 ± 0.031 | 13.78 | 0.96 |
| DAD$_{mDia3}$[a] | 164 ± 12 | 5.97 ± 0.027 | 15.07 | 0.89 |

[a] DAD$_{mDia1}$ encompasses residues 1145–1200, DAD$_{mDia2}$ residues 1004–1060, and DAD$_{mDia3}$ residues 1116–1170.

**TABLE 2**

**ITC analysis of binding of WT and mutant G proteins to WT and mutant mDia$_N$**

*N* is the stoichiometry of binding.

| Construct | $K_D$, nM | ΔH/kcal·mol$^{-1}$ | TΔS/kcal·mol$^{-1}$ | *N* |
|---|---|---|---|---|
| **mDia$_N$** | | | | |
| RhoA | 9.35 ± 2.7 | −2.8 ± 0.015 | 7.74 | 1.13 |
| RhoA F106H | 180 ± 30 | −1.4 ± 0.014 | 7.68 | 1.02 |
| Cdc42 | 7400 ± 1207 | 2.2 ± 0.232 | 9.09 | 0.99 |
| Cdc42 H104F | 133 ± 32 | −1.6 ± 0.027 | 7.62 | 0.79 |
| Rac1 | 1600 ± 4885 | 1.9 ± 0.237 | 8.30 | 0.84 |
| Rac1 H104F | 57 ± 15 | −2.68 ± 0.037 | 7.04 | 0.86 |
| **mDia$_N$-TSH** | | | | |
| RhoA | 8.6 ± 2.6 | −2.73 ± 0.015 | 8.09 | 1.01 |
| RhoA F106H | 1418 ± 342 | −0.69 ± 0.020 | 7.15 | 1.14 |
| Cdc42 | 1253 ± 86 | 3.28 ± 0.026 | 11.20 | 1.07 |
| Cdc42 H104F | 37 ± 27 | −0.67 ± 0.015 | 9.29 | 1.10 |
| Rac1 | 758 ± 138 | 1.65 ± 0.031 | 9.85 | 0.76 |
| ac1 H104F | 51 ± 22 | −2.11 ± 0.037 | 7.65 | 0.96 |

*Structure of the Cdc42·Gpp(NH)p·mDia$_N$-TSH Complex*—To analyze the structural basis of the determinants of specificity, we solved the x-ray structure of the complex between Cdc42·Gpp(NH)p and the mDia$_N$-TSH mutant. Due to the only micromolar affinity of the complex, Cdc42·Gpp(NH)p and mDia$_N$-TSH were purified separately and mixed with 1:1 stoichiometry prior to crystallization. Initial crystals of the space group P3$_2$1 were optimized to a final size of ~100 × 200 × 100 μm suitable for data collection. Molecular replacement with the RhoC·mDia$_N$ complex (PDB 1Z2C) structure as search model revealed a solution with two Cdc42·mDia$_N$-TSH complexes per asymmetric unit, which eventually was refined to 2.7 Å resolution (see Table 4 for data collection and refinement statistics). The overall structure is very similar to that of the RhoC·mDia$_N$ complex, with Cdc42 occupying the same binding site as RhoC and no appreciable differences in the GBD and the ARR subdomains (Fig. 5, *A* and *B*) reflected in the low root mean square deviation value of 1.65 Å. Superimposition of Cdc42·mDia$_N$-TSH-with the three available structures of mDia$_N$, in complex with DAD (32, 41) and with RhoC·Gpp(NH)p (35), reveals that the dimerization domain is oriented differently in each of these structures (Fig. 5*B*) due to different bending of the C-terminal half of the long helix (α17) connecting ARR and Dim (Fig. 5*C*). The orientation of Cdc42·Gpp(NH)p in the mDiaN-TSH complex is essentially the same as Rho·Gpp(NH)p in the mDia$_N$ complex (Fig. 5*B*), and the structures of both G proteins are basically identical (Fig. 5*D*).

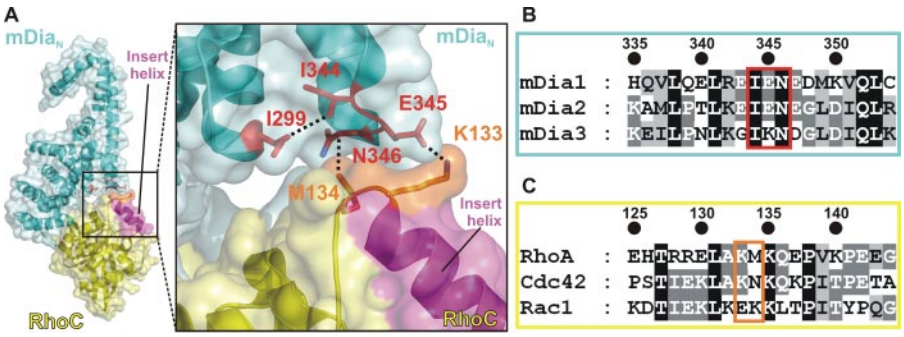


FIGURE 4. **Interaction of the Rho insert helix with mDia$_N$.** *A,* ribbon and surface representation of the RhoC·mDia$_N$ complex (PDB 1Z2C) with RhoC and mDia$_N$ in *yellow* and *cyan,* respectively, in an overview (*left section*) and as a close-up view (*right section*). The Rho insert helix is colored in *magenta* and particular residues (Lys-133 and Met-134 of RhoC and Ile-299, Ile-344, Glu-345, and Asn-346 of mDia$_N$) are highlighted as *sticks* and interactions as *dashed lines*. *B* and *C,* sequence alignment of mDia isoforms and Rho proteins (accession numbers as in Fig. 2). Residues Lys-133 and Met-134 of RhoC and Ile-299, Ile-344, Glu-345, and Asn-346 of mDia$_N$, described in the text and depicted as *sticks* in *A*, are highlighted.

It should be noted that the numbering of the Armadillo repeat

**TABLE 3**

**Stopped-flow kinetic analysis of interaction of WT and mutant Rho with $mDia_N$**

The following abbreviations are used: $k_d$, dissociation rate constant; $k_a$, association rate constant; $K_D$, $k_d/k_a$ where $K_D$ is dissociation equilibrium constant.

| Interaction partners | $k_d$/$s^{-1}$ | $k_a$/$\mu M^{-1}\cdot s^{-1}$ | $K_D$, nM |
|---|---|---|---|
| RhoA/$mDia_N$ | 0.003 | 0.497 | 6 |
| RhoA K133E/$mDia_N$ | 0.003 | 0.064 | 46 |
| RhoA M134A/$mDia_N$ | 0.002 | 0.337 | 6 |
| RhoA M134E/$mDia_N$ | 0.004 | 0.329 | 12 |
| RhoA K135A/$mDia_N$ | 0.002 | 0.458 | 4 |
| RhoA K135E/$mDia_N$ | 0.002 | 0.482 | 4 |
| RhoA/$mDia_N$ I299A | 6.76 | 0.333 | 20,300 |
| RhoA/$mDia_N$ I299E | 10.78 | 0.257 | 42,000 |
| RhoA/$mDia_N$ E345K | 0.004 | 0.473 | 8 |
| RhoA/$mDia_N$ N346A | 0.008 | 0.404 | 20 |

**TABLE 4**

**Statistics of data collection and structure refinement**

Values in parentheses correspond to those in the outer resolution shell.

| | |
|---|---|
| **Data collection** | |
| Space group | $P3_2$ |
| X-ray wavelength | 0.9763 Å |
| Unit cell dimension | $a = b = 71.27$ Å, $c = 244.96$ Å |
| Resolution (Å) | 43.5 to 2.7 Å (2.8-2.7) |
| $Rs_{ym}$[a] | 7.4 (38.1) |
| $\langle I\rangle/\sigma\langle I\rangle$ | 13.5 (3.7) |
| Completeness (%) | 99.5 (99.8) |
| No. of reflections unique | 38,038 (3,957) |
| Redundancy | 3.2 (3.2) |
| **Refinement** | |
| $R_{cryst}$[b]/$R_{free}$[c] | 20.6%/24.3% |
| No. of atoms | 8,341 |
| Proteins | 8,228 |
| Gpp(NH)p/$Mg^{2+}$ | 66 |
| Water | 47 |
| r.m.s.d.[d] bond lengths (weight) | 0.007 Å (0.022 Å) |
| r.m.s.d.[d] bond angles (weight) | 1.104° (1.998°) |
| **Ramachandran**[e] | |
| Favored | 98.9% |
| Allowed | 100.0% |

[a] $R_{sym} = (\Sigma|(I - \langle I\rangle)|)/(\Sigma I)$, where $\langle I\rangle$ is the average intensity of multiple measurements.
[b] $R_{cryst} = (\Sigma|F_{obs} - F_{calc}|)/(\Sigma|F_{obs}|)$.
[c] $R_{free}$ is the *R*-factor based on 5% of the data excluded from refinement.
[d] r.m.s.d. is root mean square deviation.
[e] Data were analyzed by MolProbity (70).

motifs has been changed compared with our earlier report (35). Because of sequence comparison with the consensus Armadillo repeat motifs, we now consider the first Armadillo repeat of $mDia_N$ to be incomplete rather then the ARM5. ARM1 contains only the second and the third $\alpha$-helices. $\alpha$17 is thus the third $\alpha$-helix of ARM5. The differences in $\alpha$17 and ARM5 positions indicate a conformational flexibility of the dimerization domain relative to the rest of the molecule.

*Structural Basis of Specificity*—A schematic summary of the interactions found in the Cdc42·$mDia_N$-TSH complex structure is given in Fig. 6*A*. The superimposition of the two complex structures reveals that the regions involved in complex formation overall align quite well. Cdc42 binds via switch I and switch II regions in a basically analogous manner as described previously for the Rho complex (34, 35). The switch I region, as already observed for the Rho complex, exclusively interacts with the GBD of mDia (Fig. 6*B*). Residue Phe-$37^C$ in switch I undergoes hydrophobic interactions with the aliphatic side chains of both Met-$115^{TSH}$ and Leu-$104^{TSH}$, although Phe-$37^C$ adapts a different rotameric conformation as compared with Phe-$39^R$ in the Rho complex. Although in the Rho complex a salt bridge is formed between Glu-$40^R$ and Lys-$107^{NNN}$, no such interaction is found for the corresponding residue Asp-$38^C$ probably due to its smaller side chain impeding a closer distance to the $\epsilon$-amino group of Lys-$107^{TSH}$ (Fig. 6*B*). In line with this, the electron density for the side chain of Lys-$107^{TSH}$ is less well defined arguing for more flexibility because of a weaker interaction. The absence of this salt bridge may thus contribute to the weaker affinity of Cdc42 to $mDia_N$-TSH as compared with Rho.

A notable feature of the switch II region is that it is invariant among Rho isoforms A–C, Cdc42, and Rac isoforms 1–3. As in the Rho complex, switch II of Cdc42 interacts with both the $GBD_N$ and the ARR subdomains. In the superimposition of the two complexes, the switch II regions almost perfectly align (Fig. 6*C*). The side chain of Asp-$67^R$ displays a polar contact to the side chain of Asn-$164^{NNN}$ in the triple NNN motif. No such interaction can be formed with Asp-$65^C$ because of the N165T mutation in $mDia_N$-TSH. Here the $\gamma$-methyl group of Thr-$164^{TSH}$ points toward the carboxyl side chain of Asp-$65^C$. The orientation of Arg-$66^C$ is almost identical to that of Arg-$68^R$, which we have previously proven to be one of the major contributors of the affinity of Rho to mDia binding (35).

The higher resolution of the Cdc42·$mDia_N$-TSH complex structure allowed us to localize protein-bound solvent. Two water molecules are coordinated in the polar interface surrounding switch II of Cdc42 and the $GBD_N$ and the ARR subdomain (Fig. 6*C*). Wat195 is coordinated by the main chain carbonyl of Thr-$164^{TSH}$ and the side chain amino group of Asn-$217^{TSH}$ and closely located to the guanidinium side chain of Arg-$66^C$. A second water molecule, Wat189, is caged by hydrogen bonds with the carbonyl oxygen of Met-$94^{TSH}$ and Asp-$63^C$ and the main chain nitrogen atom of Asp-$65^C$. Although the lower resolution of the Rho·$mDia_N$ complex structure did not reveal such details, enough space in combination with an equivalent protein anatomy is present for a similar water coordination network.

The major difference between mDia1 and mDia2/3 in the G protein binding interface is the NNN-TSH substitution. In the superimposition of the two complex structures, the NNN motif and the THS motif adapt the same backbone conformation (Fig. 6*C*). The $\gamma$-amido group of the Asn-$165^{NNN}$ side chain is involved in a polar contact to the carboxyl group of Glu-$102^R$. Furthermore, Asn-$165^{NNN}$ forms a hydrophobic interaction to Phe-$106^R$ via its $\beta$-methyl group. In contrast, Ser-$165^{TSH}$ is only involved in the formation of a nonpolar interaction with its $\beta$-methyl group and His-$104^C$. Both Asn-$166^{NNN}$ and His-$166^{TSH}$ interact via their main chain carbonyl with the side chain of Arg-$68^R$/Arg-$66^C$. The side chain of His-$166^{TSH}$ presents a more extended hydrophobic surface for interaction with His-$104^C$ compared with the smaller polar side chain of Asn-$166^{NNN}$. A space-filling representation in this area of the interface shows a better complementation with the more bulky hydrophobic side chain of His-$166^{TSH}$ compared with the smaller polar side chain of Asn-$166^{NNN}$ (Fig. 7, *A* and *B*). In the case of $mDia_N$-NNN, a tunnel large enough to harbor water molecules is located close to the hydrophobic surface created by His-$105^R$ and Phe-$106^R$ (Fig. 7*A*), whereas this tunnel is completely occluded in the Cdc42·$mDia_N$-TSH complex by the

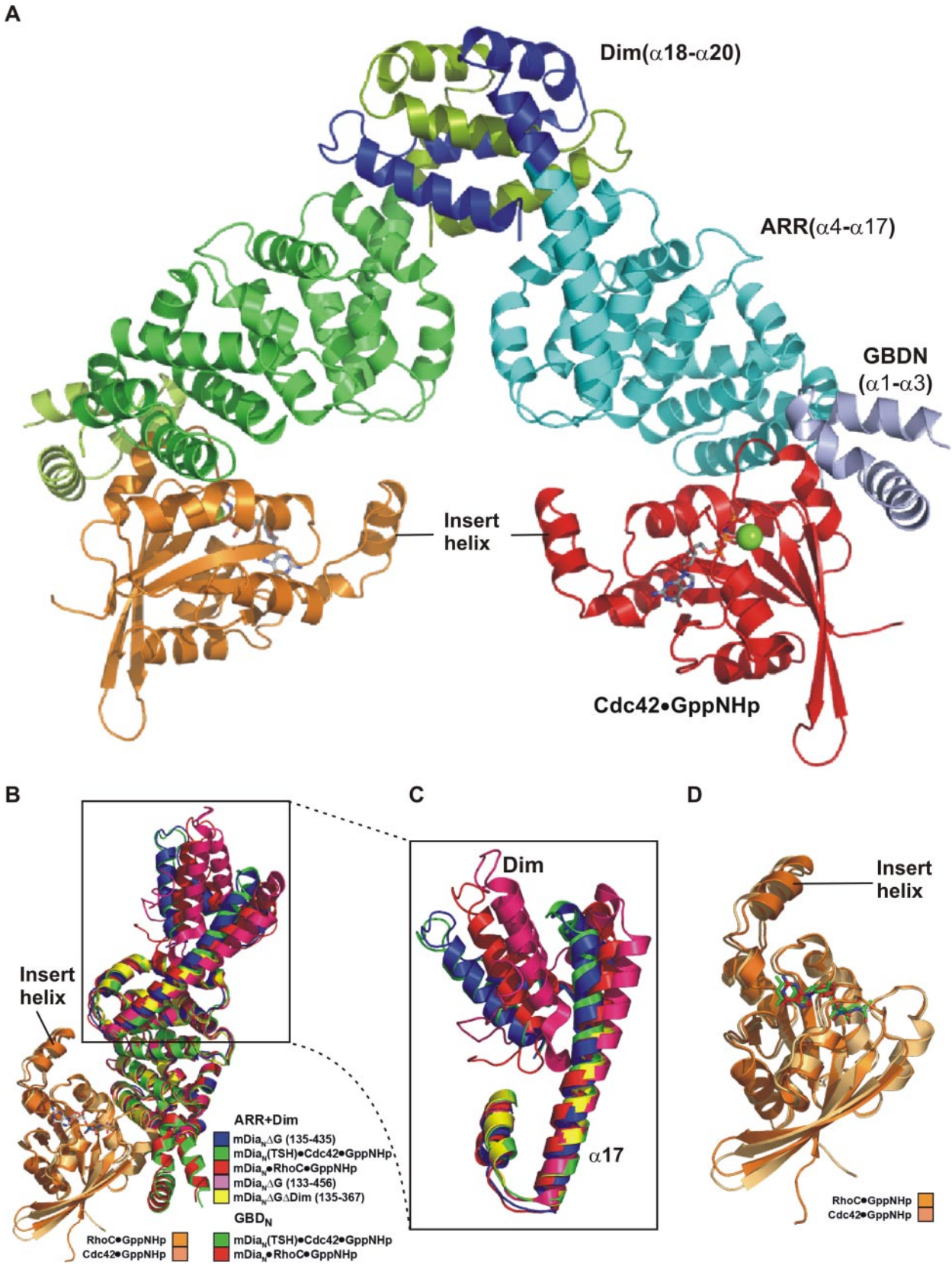


FIGURE 5. **Structure of the Cdc42·mDia$_N$-TSH complex.** *A,* ribbon and surface representation of the Cdc42·mDia$_N$-TSH dimer, with color coding as indicated, Gpp(NH)p as *stick* model and $Mg^{2+}$ ions as *green spheres. B,* superimposition of the Cdc42·mDia$_N$-TSH complex structure (mDia$_N$-TSH colored in *green* and Cdc42 in *pale orange*) with RhoC·mDia$_N$ complex (PDB 1Z2C, mDia$_N$ colored in *red* and RhoC colored in *orange*), mDia$_N$ of mDia$_N$·DAD complex (PDB 2BAP, mDia$_N$ colored in *blue*), mDia-(131–516) (PDB 2BNX (46), colored in *magenta*), and mDia1-(135–367) (PDB 2F31 (44), colored in *yellow*). *C,* close-up view of the superimposition from *B,* highlighting the long helix α17, helix 3 of the of the fifth ARM of ARR, and the dimerization domain (*Dim*). *D,* close up view of the superimposition from *B* showing Cdc42 and RhoC (color coding as in *B*) with the Gpp(NH)p molecules as *sticks*.

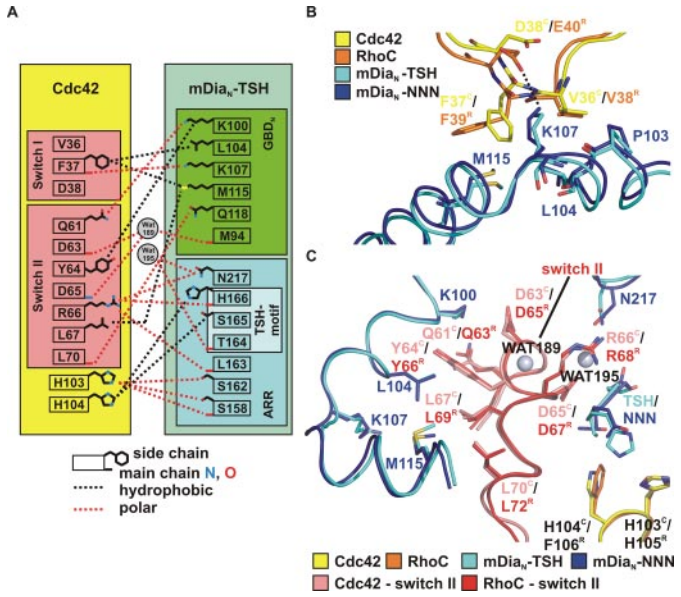


FIGURE 6. **Structural analysis of the Cdc42 mDia$_N$-TSH interaction.** *A,* schematic drawing of interacting residues in Cdc42 and mDia$_N$-TSH (cutoff distance 3.6 Å). *B,* superimposition of the Cdc42 and the RhoC complexes in the contact area of switch I and mDia$_N$ (color legend in figure), highlighting particular residues, including the salt bridge between Glu40$^R$ and Lys-107$^{NNN}$. *C,* superimposition of the Cdc42 and the RhoC complexes in the contact area of switch II (color legend in figure), with water molecules displayed as *gray spheres* and with selected residues highlighted as *sticks*. For clarity, only important parts of mDia$_N$-TSH and Cdc42 are displayed. The switch II region of RhoC and Cdc42 is highlighted in *red* and *salmon*, respectively.

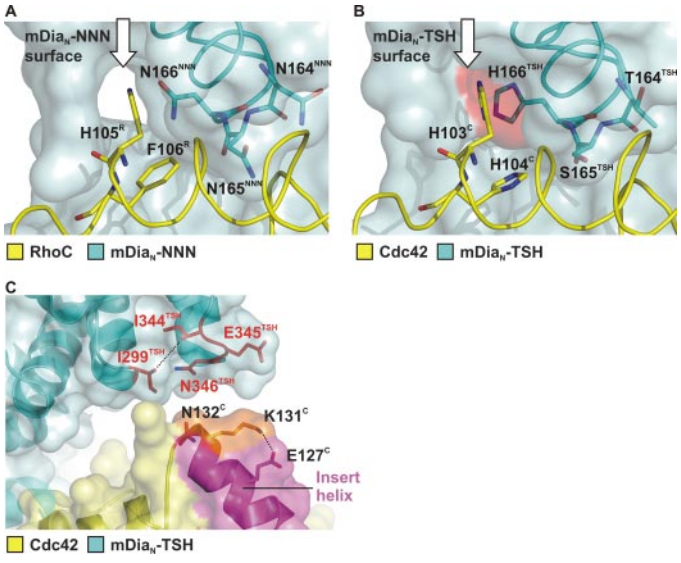


FIGURE 7. **Structural basis of specificity.** *A* and *B,* superimposition the Cdc42 and RhoC complexes with WT and mDia$_N$-TSH around the central portion around the NNN/TSH- motifs, with color coding as indicated. The G proteins are displayed as *ribbons* on a transparent surface of WT (*A*) or TSH- mutant (*B*) mDia$_N$, with the NNN and TSH motifs (in *blue sticks*) shining through. The *white arrow* points to a solvent-accessible tunnel present in the RhoC·mDia$_N$-NNN structure (*A*), which is closed by the larger side chain of His-166$^{TSH}$ in the Cdc42·mDia$_N$-TSH structure (*B*). The additional van der Waals surface provided by the larger His-166$^{TSH}$ side chain is highlighted in *red*. (*B*). *C,* ribbon and surface representation of the Cdc42·mDia$_N$-TSH complex around the Cdc42 insert helix, with color coding as indicated and special residues highlighted in *stick* representation. The Cdc42 insert helix is highlighted in *magenta*, and residues Lys-131$^C$ and Asn-132$^C$ are colored in *orange* (compare Fig. 4).

bulkier side chain of H166$^C$, which creates a continuous hydrophobic surface (Fig. 7*B*). We thus believe that the more extended hydrophobic surface offered to His-103$^C$ and His-104$^C$, the better space complementation and the occlusion of a solvent-filled tunnel in the Cdc42-binding surface on mDia are responsible for the increased affinity of Cdc42 toward mDia$_N$-TSH.

Although the Rho·mDia$_N$ complex shows an additional contact between the C-terminal end of the Rho insert helix and the ARR (Fig. 4*A*), no such interaction is present in the Cdc42·mDia$_N$-TSH complex structure, and the distance between the corresponding elements is longer (Fig. 5, *B* and *D*, and Fig. 7*C*). Instead, the ϵ-amino group of Lys-131$^C$ forms an intramolecular salt bridge with Glu-127$^C$ thereby neutralizing the positive charge of Lys-131$^C$. In contrast, the residue corresponding to Glu-127$^C$ is Arg-129$^R$, which might even amplify the positive charge on Lys-133$^R$ thus strengthening the ionic interaction with Glu-345$^{NNN}$ (compare Fig. 4*C*). Notably, in Rac1 Arg-129$^R$ is replaced by Glu-127$^{Rac}$, and Lys-133$^R$ is replaced by the negatively charged Glu-131$^{Rac}$ and could thus be responsible for the differences in binding affinity toward mDia isoforms.

## DISCUSSION

Here we have extended our analysis of the interaction of the N-terminal part of mDia with their cognate G proteins and whether this affects the auto-inhibitory regulation of these formins. We have furthermore dissected the molecular details of the interface between Rho proteins and mDia to derive explanations for the specificity of their interactions.

First, we show that the C-terminal polybasic region of the C-terminal auto-inhibitory region does not overlap with the G protein-binding site. In previous structures of the mDia$_N$·DAD complexes (32, 41), only 16 residues comprising the DCR forming an amphipathic helix were visible. Mutational analysis shows that the effect of mutating the negative charges C-terminal to the DCR has an additive effect on the affinity of a DAD peptide for the N terminus. Although the release of autoinhibition by the binding of Rho is mediated by the mutual exclusive binding of the core DAD region and G proteins, as analyzed previously by biochemistry and structure (32, 40, 41), our studies here further confirm and extend previous assumptions that the binding sites of G proteins and DAD relevant for affinity are only partially overlapping. The mutations in the polybasic DAD-binding region on mDia$_N$ did not influence Rho binding (RhoA-mDia$_N$ E358R/E362R, 9 nM; RhoA-mDia$_N$ E358R/E362R/E366R, 16 nM; data not shown). This is strengthened by our biochemical data that show that any of the mutations that influence specificity and affinity of Rho binding have almost no effect on DAD binding (Table 1) (32, 35). It should be added that the DAD regions of mDia1, -2, and -3 are sufficiently conserved, such that they bind with almost equal affinity to the N-terminal part of mDia1, such that inhibition in *trans* between mDia isoforms cannot be excluded (Table 1).

We also show that Cdc42 binds in exactly the same position as Rho and that the specificity of interaction between Rho, Rac, Cdc42 *versus* mDia1, -2, and -3 isoforms is mediated mostly by two surface epitopes in the complex interface. Surprisingly, the specificity is not dictated by sequence differences in the switch regions even though both of them are involved in the interaction but is in line with the high sequence conservation of the

switches. A minor contribution to specificity comes from the switch I residue Glu-40 in Rho, which in Rac and Cdc42 is Asp-38. Switch II is completely conserved between Rho, Rac, and Cdc42 and is involved in a large number of interactions.

The first specificity epitope occurs in the central portion of the interface where the mDia1 NNN motif is replaced by the TSH motif of mDia2 and -3. The crucial Arg-68$^{R}$ residue in switch II, which inserts like a wedge into the interface formed between GBD and ARR subdomains, is one of the most important mediators of the interaction and is conserved as Arg-66 in Rac/Cdc42. The substitution relevant for affinity and specificity is the replacement of Phe-106 by His-104 in Cdc42/Rac. The structural analysis shows that the structures of the NNN and TSH motifs, which form a loop connecting the third helix of ARM1 and the first helix of the ARM2 of the mDia$_N$ ARR, superimpose very well. The major effect of the replacements seems to be a more complementary interface that is formed when His-104$^{C}$ points toward the TSH rather than the NNN module. In the latter case a solvent-accessible tunnel remains in the interface and would thus trap water molecules in the Cdc42-mDia1 interface which would be negatively affecting the affinity. Our data also show that the Phe-106 residue in this part of the interface is more important for high affinity than the NNN motif, because its introduction into Rac increases affinity drastically, whereas the effect is less pronounced in Cdc42.

The second epitope involved in specificity is formed by the Rho insert helix that contacts the ARR subdomain at the loop connecting $\alpha$16 and $\alpha$17 of ARM5 of mDia$_N$. The insert helix is a particular feature unique to the Rho subfamily of the Ras superfamily. Although the Rho insert helix has been implicated previously to be involved in a number of biological effects, *i.e.* the interaction of Rac with the NADPH oxidase (73) or for Rho kinase activation by RhoA (74) and to be essential for membrane ruffling (75), no structural analysis has yet shown such an interaction. The evidence for the involvement of the insert helix has mostly come from deletion experiments that may or may not produce a proper folding protein.[4] The analysis here shows for the first time that the insert helix makes a substantial contribution to the affinity but may be even more important for the specificity. Although the interface between Rho and mDia1 is very tight and complementary, the interface between Cdc42 and the mDia-TSH mutant leaves much space between the corresponding epitopes. Although the difference in complementarity cannot directly be assigned to particular residues, the sequence differences in the area are sufficiently different between the three mDia isoforms to assume a significantly different surface. Our mutational analysis shows that residues apparently not directly involved in this interface have nevertheless a large effect on binding affinity. We can thus speculate that the replacement of the contact area by the respective sequences from mDia2 and -3 would, in conjunction with the TSH motif, create a high affinity protein for Rac and/or Cdc42.

Previously, we have shown that Rho actively displaces DAD from binding to the N-terminal region of mDia (34). Due to the partial overlap of Rho·GTP and DAD, we have postulated a two-step binding mechanism in which the G protein makes a preliminary contact for a loosely bound complex in a first step. In a second step, steric interference and charge-charge repulsion lead to dissociation of DAD and formation of a tight complex. In such a scenario, the Rho insert helix might thus make a first weak interaction which, however, already differentiates between the Rho isoforms RhoA, -B, and -C and Cdc42/Rac. The second step involves the central portion of the interface, where the interaction with the NNN or TSH motif leads to a tight binding complex where DAD is released and the FH2 domain is ready to polymerize actin. Whether or not the FH2 domains, once released from auto-inhibited mDia, have the same activity toward actin polymerization remains to be determined.

*Acknowledgments—We are grateful to the machine and beamline groups whose outstanding efforts have made these experiments possible. We thank Andrea Scrima and Wulf Blankenfeldt for data collection.*

[4] R. Ahmadian, unpublished observations.

## REFERENCES


1. Castrillon, D. H., and Wasserman, S. A. (1994) *Development* (*Camb.*) **120,** 3367–3377
2. Pantaloni, D., Le Clainche, C., and Carlier, M. F. (2001) *Science* **292,** 1502–1506
3. Pollard, T. D., and Borisy, G. G. (2003) *Cell* **112,** 453–465
4. Bompard, G., and Caron, E. (2004) *J. Cell Biol.* **166,** 957–962
5. Buck, M., Xu, W., and Rosen, M. K. (2004) *J. Mol. Biol.* **338,** 271–285
6. Eden, S. R., Rohatgi, A. V., Podtelejnikov Mann, M., and Kirschner, M. W. (2002) *Nature* **418,** 790–793
7. Pruyne, D., Evangelista, M., Yang, C., Bi, E., Zigmond, S. H., Bretscher, A., and Boone, C. (2002) *Science* **297,** 612–615
8. Quinlan, M. E., Heuser, J. E., Kerkhoff, E., and Mullins, R. D. (2005) *Nature* **433,** 382–388
9. Evangelista, M., Zigmond, S., and Boone, C. (2003) *J. Cell Sci.* **116,** 2603–2611
10. Higgs, H. N. (2005) *Trends Biochem. Sci.* **30,** 342–353
11. Romero, S., Le Clainche, C., Didry, D., Egile, C., Pantaloni, D., and Carlier, M. F. (2004) *Cell* **119,** 419–429
12. Wallar, B. J., and Alberts, A. S. (2003) *Trends Cell Biol.* **13,** 435–446
13. Zigmond, S. H., Evangelista, M., Boone, C., Yang, C., Dar, A. C., Sicheri, F., Forkey, J., and Pring, M. (2003) *Curr. Biol.* **13,** 1820–1823
14. Kato, T., Watanabe, N., Morishima, Y., Fujita, A., Ishizaki, T., and Narumiya, S. (2001) *J. Cell Sci.* **114,** 775–784
15. Ozaki-Kuroda, K., Yamamoto, Y., Nohara, H., Kinoshita, M., Fujiwara, T., Irie, K., and Takai, Y. (2001) *Mol. Cell. Biol.* **21,** 827–839
16. Zigmond, S. H. (2004) *Curr. Opin. Cell Biol.* **16,** 99–105
17. Harris, E. S., Li, F., and Higgs, H. N. (2004) *J. Biol. Chem.* **279,** 20076–20087
18. Higgs, H. N., and Peterson, K. J. (2005) *Mol. Biol. Cell* **16,** 1–13
19. Pring, M., Evangelista, M., Boone, C., Yang, C., and Zigmond, S. H. (2003) *Biochemistry* **42,** 486–496
20. Shimada, A., Nyitrai, M., Vetter, I. R., Kuhlmann, D., Bugyi, B., Narumiya, S., Geeves, M. A., and Wittinghofer, A. (2004) *Mol. Cell* **13,** 511–522
21. Xu, Y., Moseley, J. B., Sagot, I., Poy, F., Pellman, D., Goode, B. L., and Eck, M. J. (2004) *Cell* **116,** 711–723
22. Higashida, C., Miyoshi, T., Fujita, A., Oceguera-Yanez, F., Monypenny, J., Andou, Y., Narumiya, S., and Watanabe, N. (2004) *Science* **303,** 2007–2010
23. Kovar, D. R., and Pollard, T. D. (2004) *Nat. Cell Biol.* **6,** 1158–1159
24. Kovar, D. R., Wu, J. Q., and Pollard, T. D. (2005) *Mol. Biol. Cell* **16,** 2313–2324
25. Li, F., and Higgs, H. N. (2003) *Curr. Biol.* **13,** 1335–1340
26. Shemesh, T., Otomo, T., Rosen, M. K., Bershadsky, A., and Kozlov, M. M.

(2005) *J. Cell Biol.* **170,** 889–893
27. Wear, M. A., Yamashita, A., Kim, K., Maéda, Y., and Cooper, J. A. (2003) *Curr. Biol.* **13,** 1531–1537
28. Otomo, T., Tomchick, D. R., Otomo, C., Panchal, S. C., Machius, M., and Rosen, M. K. (2005) *Nature* **433,** 488–494
29. Bedford, M. T., Chan, D. C., and Leder, P. (1997) *EMBO J.* **16,** 2376–2383
30. Macias, M. J., Wiesner, S., and Sudol, M. (2002) *FEBS Lett.* **513,** 30–37
31. Alberts, A. S. (2001) *J. Biol. Chem.* **276,** 2824–2830
32. Lammers, M., Rose, R., Scrima, A., and Wittinghofer, A. (2005) *EMBO J.* **24,** 4176–4187
33. Otomo, T., Otomo, C., Tomchick, D. R., Machius, M., and Rosen, M. K. (2005) *Mol. Cell.* **18,** 273–281
34. Rose, R., Wittinghofer, A., and Weyand, M. (2005) *Acta Crystallogr. F Struct. Biol. Crystalliz. Comm.* **61,** 225–227
35. Rose, R., Weyand, M., Lammers, M., Ishizaki, T., Ahmadian, M. R., and Wittinghofer, A. (2005) *Nature* **435,** 513–518
36. Watanabe, N., Madaule, P., Reid, T., Ishizaki, T., Watanabe, G., Kakizuka, A., Saito, Y., Nakao, K., Jockusch, B. M., and Narumiya, S. (1997) *EMBO J.* **16,** 3044–3056
37. Copeland, J. W., and Treisman, R. (2002) *Mol. Biol. Cell* **13,** 4088–4099
38. Ishizaki, T., Morishima, Y., Okamoto, M., Furuyashiki, T., Kato, T., and Narumiya, S., (2001) *Nat. Cell Biol.* **3,** 8–14
39. Watanabe, N., Kato, T., Fujita, A., Ishizaki, T., and Narumiya, S. (1999) *Nat. Cell Biol.* **1,** 136–143
40. Li, F., and Higgs, H. N. (2005) *J. Biol. Chem.* **280,** 6986–6992
41. Nezami, A., Poy, F., and Eck, M. (2006) *Structure* (*Lond.*) **14,** 257–263
42. Ihara, K., Muraguchi, S., Kato, M., Shimizu, T., Shirakawa, M., Kuroda, S., Kaibuchi, K., and Hakoshima, T. (1998) *J. Biol. Chem.* **273,** 9656–9966
43. Pai, E. F., Kabsch, W., Krengel, U., Holmes, K. C., John, J., and Wittinghofer, A. (1989) *Nature* **341,** 209–214
44. Vetter, I. R., and Wittinghofer, A. (2001) *Science* **294,** 1299–1304
45. Wittinghofer, A., and Pai, E. F. (1991) *Trends Biochem. Sci.* **16,** 382–387
46. Arai, R., and Mabuchi, I. (2002) *J. Cell Sci.* **115,** 887–898
47. Bishop, A. L., and Hall, A. (2000) *Biochem. J.* **348,** 241–255
48. Etienne-Manneville, S., and Hall, A. (2002) *Nature* **420,** 629–635
49. Ho, H. Y., Rohatgi, R., Lebensohn, A. M., Ma, L., Li, J., Gygi, S. P., and Kirschner, M. W. (2004) *Cell* **118,** 203–216
50. Raftopoulou, M., and Hall, A. (2004) *Dev. Biol.* **265,** 23–32
51. Ridley, A. J., and Hall, A. (1992) *Cell* **70,** 389–399
52. Takai, Y., Sasaki, T., Tanaka, K., and Nakanishi, H. (1995) *Trends Biochem. Sci.* **20,** 227–231
53. Wennerberg, K., and Der, C. J. (2004) *J. Cell Sci.* **117,** 1301–1312
54. Burbelo, P. D., Drechsel, D., and Hall, A. (1995) *J. Biol. Chem.* **270,** 29071–29074
55. Jacobs, M., Hayakawa, K., Swenson, L., Bellon, S., Fleming, M., Taslimi, P., and Doran, J. (2006) *J. Biol. Chem.* **281,** 260–268
56. Maesaki, R., Ihara, K., Shimizu, T., Kuroda, S., Kaibuchi, K., and Hakoshima, T. (1999) *Mol. Cell* **4,** 793–803
57. Leung, D. W., and Rosen, M. K. (2005) *Proc. Natl. Acad. Sci. U. S. A.* **102,** 5685–5690
58. Van Aelst, L., and D'Souza-Schorey, C. (1997) *Gen. Dev.* **11,** 2295–2322
59. Dvorsky, R., and Ahmadian, M. R. (2004) *EMBO Rep.* **12,** 1130–1136
60. Matsui, T., Amano, M., Yamamoto, T., Chihara, K., Nakafuku, M., Ito, M., Nakano, T., Okawa, K., Iwamatsu, A., and Kaibuchi, K. (1996) *EMBO J.* **15,** 2208–2216
61. Leung, T., Chen, X. Q., Manser, E., and Lim, L. (1996) *Mol. Cell. Biol.* **16,** 5313–5327
62. Gasman, S., Kalaidzidis, Y., and Zerial, M. (2003) *Nat. Cell Biol.* **5,** 195–204
63. Yasuda, S., Oceguera-Yanez, F., Kato, T., Okamoto, M., Yonemura, S., Terada, Y., Ishizaki, T., and Narumiya, S. (2004) *Nature* **428,** 767–771
64. Wiseman, T., Williston, S., Brandts, J. F., and Lin, L. N. (1989) *Anal. Biochem.* **179,** 131–137
65. Kabsch, W. (1993) *J. Appl. Crystallogr.* **26,** 795–800
66. Vagin, A., and Teplyakov, A. (1997) *J. Appl. Crystallogr.* **20,** 1022–1025
67. Brünger, A. T., Krukowski, A., and Erickson, J. W. (1990) *Acta Crystallogr.* **46,** 585–593
68. Emsley, P., and Cowtan, K. (2004) *Acta Crystallogr.* **60,** 2126–2132
69. Murshudov, G. N., Lebedev, A., Vagin, A. A., Wilson, K. S., and Dodson, E. J. (1999) *Acta Crystallogr.* **55,** 247–255
70. Lovell, S. C., Davis, I. W., Arendall, W. B., III, de Bakker, P. I., Word, J. M., Prisant, M. G., Richardson, J. S., and Richardson, D. C. (2003) *Proteins Struct. Funct. Genet.* **50,** 437–450
71. DeLano, W. L. (2002) *The PyMOL User's Manual*, DeLano Scientific, San Carlos, CA
72. Frisch, C., Schreiber, G., Johnson, C. M., and Fersht, A. R. (1997) *Mol. Biol.* **267,** 696–706
73. Freeman, J. L., and Lambeth, J. D. (1996) *J. Biol. Chem.* **271,** 22578–22582
74. Zong, H., Kaibuchi, K., and Quilliam, L. A. (2001) *Mol. Cell. Biol.* **21,** 5287–5298
75. Karnoub, A. E., Der, C. J., and Campbell, S. L. (2001) *Mol. Cell. Biol.* **21,** 2847–2857